J Ther Eng, Vol. 10, No. 6, pp. 1494−1508, November, 2024

Journal of Thermal Engineering
Web page info: https://jten.yildiz.edu.tr
DOI: 10.14744/thermal.0000890

Research Article

A three-velocity three-temperature three-concentration description for MHD double-diffusive free convection in a cavity occupied by a tridisperse porous medium

Iman ZAHMATKESH[1,*]

[1]*Department of Mechanical Engineering, Mashhad Branch, Islamic Azad University, Mashhad, 9187147578, Iran*

ARTICLE INFO

Article history
Received: 12 September 2023
Revised: 18 December 2023
Accepted: 23 December 2023

Keywords:
Free Convection; Heat Transfer; Magnetohydrodynamics; Mass Transfer; Tridisperse Porous Media (TDPM)

ABSTRACT

This work proposes a three-velocity three-temperature three-concentration (3V-3T-3C) model to describe the momentum, energy, and mass transfer in the macro-pores, meso-pores, and micro-pores in a tridisperse porous medium (TDPM), in the attendance of magnetic field imposition. Thereafter, the system of these highly coupled equations is solved numerically to scrutinize MHD double-diffusive free convection heat transfer in a square cavity occupied by a TDPM, for the first time. Finally, features of the pertinent parameters on the flow strength as well as heat and mass transfer are disclosed through contour plots and tables. The simulation results suggest that the elimination of the magnetic field as well as increase in the double-diffusion ratio boosts up the flow strength and embellishes the heat and mass transfer, in all scales of porosity of the TDPM. It is also scrutinized that rise in the Lewis number is accompanied by small declination in the flow strength and the heat transfer and substantial elevation in the mass transfer, in all scales of porosity. Meanwhile, the consequences of the magnetic field imposition, the double-diffusion ratio, and the Lewis number are detected to be more intense in the macro-pores, as compared with the other scales of porosity of the TDPM. Additionally, it is elucidated that change in the macro-porosity is more likely to alter the heat and mass transfer performances, as compared with the meso-porosity or micro-porosity.

Cite this article as: Zahmatkesh I. A three-velocity three-temperature three-concentration description for MHD double-diffusive free convection in a cavity occupied by a tridisperse porous medium. J Ther Eng 2024;10(6):1494−1508.

INTRODUCTION

Bidisperse porous media have been introduced as extension of traditional mono-dispersed porous materials. They comprise two scales of porosity, namely, macro-pores and micro-pores. Physically, a bidisperse medium (BDPM) is a composition of clusters of large particles that are themselves agglomerations of small particles. Here, the macro-pores are represented by spaces between the clusters and the micro-pores are characterized by spaces within the clusters. Thereby, one may look at a BDPM as a traditional porous medium in which the solid phase is replaced by another porous medium with smaller pores. As a consequence of the

***Corresponding author.**
*E-mail address: Zahmatkesh5310@mshdiau.ac.ir, iman.zahmatkesh@gmail.com

This paper was recommended for publication in revised form by Editor-in-Chief Ahmet Selim Dalkılıç

Published by Yıldız Technical University Press, İstanbul, Turkey

enhanced surface area, bidisperse porous materials appear in bidisperse adsorbent and bidisperse capillary wicks in heat pipes. Moreover, flow and thermal fields in data centers having densely packed heat generating devices can be simulated through the equations governing bidisperse porous materials [1].

The first study on bidisperse porous materials was reported by Chen *et al.* [2]. They performed an experimental work on boiling heat transfer in a channel occupied by sintered copper bidisperse porous materials. Their results demonstrated the suitability of bidisperse porous materials for flow boiling at high heat fluxes, as compared with the traditional mono-dispersed porous materials. After this pioneering endeavor, much effort has been devoted to the simulation of bidisperse porous materials in the context of forced and free convection heat transfer. Nield and Kuznetsov [3, 4] derived a two-velocity two-temperature model for a BDPM and applied it to fully-developed flow in a channel. Thereafter, they utilized it to study thermally developing flow in a channel [5], the onset of convection heat transfer in a horizontal layer heated from below [6, 7], and free convection heat transfer along a vertical plate [8] in bidisperse porous materials. Further, they scrutinized forced convection heat transfer in a channel partly occupied by bidisperse porous materials in symmetric and asymmetric [9] circumstances. Meanwhile, Rees *et al.* [10] and Cheng [11] analyzed free convection boundary-layer flow in bidisperse porous materials. Revnic *et al.* [12] and Narasimhan and Reddy [13] studied free convection heat transfer in a square cavity occupied by a BDPM. Wang *et al.* [14] discussed forced convection heat transfer in a BDPM embedded in a circular pipe. Straughan [15] simulated convection heat transfer in an anisotropic BDPM. Capone and De Luca [16] analyzed the onset of convection heat transfer in a uniformly-rotating horizontal porous layer occupied by a BDPM and heated from below. In another attempt [17], they discussed the flow instability in a horizontal BDPM, heated from below. Wang *et al.* [18] accomplished analytic solution for forced convection heat transfer in an annular duct filled with a BDPM subjected to asymmetric heat fluxes. More recently, Siddabasappa *et al.* [19] reported linear and weakly nonlinear stability analyses of Brinkman-Benard convection in a BDPM.

Meza *et al.* [20] and Rys *et al.* [21] fabricated lattices comprising three scales of porosity, namely, macro-pores, meso-pores, and micro-pores, which represent a tridisperse porous medium (TDPM). However, there is a noticeable dearth of works in flow and thermal fields as well as heat and mass transfer characteristics inside a TDPM. Some available works are as follows:

Nield and Kuznetsov [22] extended their two-velocity two-temperature model to a three-velocity three-temperature model to describe a TDPM and applied it to simulated forced convection heat transfer in a channel with uniform temperature or uniform heat flux at the walls. Thereafter, they scrutinized the onset of convection heat transfer [23] and free convection heat transfer along a vertical plate [24] in tridisperse porous materials. Meanwhile, free convection heat transfer about a vertical cone embedded in a TDPM was discussed by Cheng [25]. In these studies, it was noticed that any elevation in the permeability ratios or the modified thermal conductivity ratios intensities the heat transfer rate in tridisperse porous materials. In another attempt, Ghalambaz *et al.* [26] simulated free convection heat transfer in a square cavity occupied by a TDPM. They reported that the mean Nusselt number was an increasing function of the thermal conductivity ratios and the permeability ratios and a deceasing function of the inter-phase momentum transfer coefficient.

Double-diffusive free convection induced by both temperature and solute concentration gradients is often accompanied by special features which make them distinct from the flows driven by a single buoyancy effect. This phenomenon appears in many practical processes including material drying, wet cooling towers, packed bed catalytic reactors, enhanced oil recovery, and water evaporation from its free surface. Going to the literature indicates many previous endeavors on double-diffusive convection heat transfer in porous media. Examples includes the studies Umavathi and Sheremet [27], Aly *et al.* [28], Habibi and Zahmatkesh [29], and Zahmatkesh and Shandiz [30]. Meanwhile, triple-diffusive convection heat transfer in porous cavities was analyzed by Ghalambaz *et al.* [31, 32] and Khan *et al.* [33].

Recently, Straughan [34], Wang *and Wang.* [35], Badday and Harfash [36, 37], and Ramchandraiah *et al.* [38] have studied double-diffusive heat transfer in bidisperse porous materials. Straughan [34] studied the effect of inertia term in the momentum equation on the onset of double-diffusive convection heat transfer in a layer occupied by a BDPM heated and salted from below. Meanwhile, Wang and Wang [35] analyzed fully-developed forced convection heat and mass transfer in a channel occupied by a BDPM in the presence of chemical reaction on the wall. Additionally, Badday and Harfash [36, 37] and Ramchandraiah *et al.* [38] presented stability analysis for double-diffusive heat transfer in bidisperse porous materials. In spite of these works, double-diffusive heat transfer in a TDPM has not been discussed thus far. Similar to momentum and heat transfer, mass transfer in a TDPM occurs in the three scales of porosity, necessitating the development of a three-velocity three-temperature three-concentration model for its description.

Another important effect in porous materials goes back to the exertion of an external magnetic field, which tends to affect the flow velocities. This in turns alters the heat and mass transfer characteristics. Previous evidences demonstrate that the way in which the applied magnetic field influences the momentum, heat, and mass transfer is dependent to its intensity and orientation. In spite of previous works on MHD heat transfer in porous media (e.g., Wakif *et al.* [39], Sheremet *et al.* [40], Krishna and Chamkha [41], Ghalambaz *et al.* [42], Zahmatkesh *et al.* [43, 44], and

Ragupathi *et al.* [45], Ouni *et al.* [46], [47]), this effect has not been discussed in a BDPM or a TDPM thus far.

The particular behavior of MHD double-diffusive free convection heat transfer occurring in a TDPM motivates this work. To this aim, the three-velocity three-temperature model proposed by Nield and Kuznetsov [22] is extended to a three-velocity three-temperature three-concentration (3V-3T-3C) model. Additionally, the effect of an externally applied magnetic field is applied to the developed equations. The resulting equations are then solved to analyze MHD double-diffusive free convection heat transfer in a square cavity occupied by a TDPM. As far as we know, this problem has not been considered before. Hence, this work is original and new.

PROBLEM STATEMENT

Free convection heat transfer in a square cavity occupied by a TDPM in the attendance of magnetic field and double-diffusion is scrutinized in this study. Details of the geometry for the current flow problem are demonstrated in Figure 1. Here, the left wall is kept at the hot temperature, T_H, and the higher solute concentration, C_H, whereas the right wall is maintained at the cold temperature, T_C, and the lower concentration, C_C. Meanwhile, the top and bottom walls are adiabatic and impermeable to mass transfer.

The gravity force is acting downward. Meanwhile, a uniform magnetic field of $\boldsymbol{B} = B_x\hat{\boldsymbol{e}}_x + B_y\hat{\boldsymbol{e}}_y$ is applied to the cavity in a way that the magnetic field orientation forms an arbitrary angle of λ with the horizontal direction. The exertion of the magnetic field to a TDPM leads to the appearance of the Lorentz force, $\sigma_i(\boldsymbol{V_i} \times \boldsymbol{B}^2)$, in the momentum equation of each scale of porosity, *i*. Here, σ_i and $\boldsymbol{V_i} = u_i\hat{\boldsymbol{e}}_x + v_i\hat{\boldsymbol{e}}_y$ are the electrical conductivity of the fluid and the velocity vector in the corresponding porosity scale.

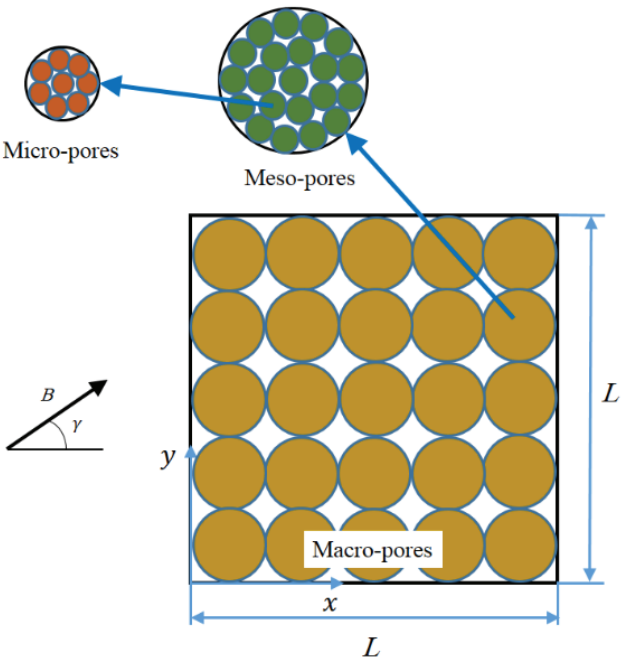

Figure 1. Details of the geometry for the current flow problem.

It is anticipated that: (a) The TDPM is isotropic and homogenous. (b) The fluid properties in the TDPM are constant. (c) The flow field in each porosity scale is 2D, steady, incompressible, Newtonian, and laminar. (d) The Darcy relation and the Boussinesq approximation adequately describe the momentum transfer in each porosity scale. (e) The contributions of viscous dissipation, radiation exchange, Soret and Dufour effects, Joule heating phenomenon, and the induced magnetic field are not significant in the TDPM. (f) The three scales of porosity in the TDPM possess similar values of pressure, viscosity, and expansion coefficients [22]. (g) During the double-diffusive free convection, the fluid density appearing in buoyancy terms of the porosity scales obeys the following role:

$$\rho = \rho_0 g[\beta_T(\bar{T} - T_C) + \beta_C(C - C_C)] \tag{1}$$

Here, ρ_0 is the reference density, β_T is the thermal expansion coefficient, and β_C is the solute concentration expansion coefficient. Moreover, $\bar{T}$ is the volume-averaged temperature and $\bar{C}$ is the volume-averaged concentration:

$$\bar{T} = \frac{\phi_1 T_1 + (1-\phi_1)\phi_2 T_2 + (1-\phi_1)(1-\phi_2)\phi_3 T_3}{\phi_1 + (1-\phi_1)\phi_2 + (1-\phi_1)(1-\phi_2)\phi_3} \tag{2}$$

$$\bar{C} = \frac{\phi_1 C_1 + (1-\phi_1)\phi_2 C_2 + (1-\phi_1)(1-\phi_2)\phi_3 C_3}{\phi_1 + (1-\phi_1)\phi_2 + (1-\phi_1)(1-\phi_2)\phi_3} \tag{3}$$

In the above relations, T_i, C_i, and ϕ_i are the temperature, the solute concentration, and the porosity in each scale of porosity in the TDPM.

Mathematical Formulation

The equations which govern the MHD double-diffusive free convection in the cavity occupied by the TDPM take the following form. It is noteworthy that this three-velocity three-temperature three-concentration (3V-3T-3C) model is an extension of the equations proposed by Nield and Kuznetsov [22] to include the effect of magnetic field and double-diffusion:

Macro-pores (Size 1)

$$\frac{\partial u_1}{\partial x} + \frac{\partial v_1}{\partial y} = 0 \tag{4}$$

$$\frac{\partial p}{\partial x} = -\frac{\mu}{K_1}u_1 + \sigma_1 B^2(v_1 \sin\lambda \cos\lambda - u_1 \sin^2\lambda) + \zeta_{12}(u_2 - u_1) \tag{5}$$

$$\frac{\partial p}{\partial y} = -\frac{\mu}{K_1}v_1 + \rho_0 g[\beta_T(\bar{T} - T_C) + \beta_C(\bar{C} - C_C)] + \sigma_1 B^2(u_1 \sin\lambda \cos\lambda - v_1 \cos^2\lambda) + \zeta_{12}(v_2 - v_1) \tag{6}$$

$$\phi_1\rho_1 c_1\left(u_1\frac{\partial T_1}{\partial x}+v_1\frac{\partial T_1}{\partial y}\right)=\phi_1 k_1\left(\frac{\partial^2 T_1}{\partial x^2}+\frac{\partial^2 T_1}{\partial y^2}\right)+h_{12}(T_2-T_1) \quad (7)$$

$$\phi_1\left(u_1\frac{\partial C_1}{\partial x}+v_1\frac{\partial C_1}{\partial y}\right)=\phi_1 D_1\left(\frac{\partial^2 C_1}{\partial x^2}+\frac{\partial^2 C_1}{\partial y^2}\right)+\xi_{12}(C_2-C_1) \quad (8)$$

Meso-pores (Size 2)

$$\frac{\partial u_2}{\partial x}+\frac{\partial v_2}{\partial y}=0 \quad (9)$$

$$\frac{\partial p}{\partial x}=-\frac{\mu}{K_2}u_2+\sigma_2 B^2(v_2\,sin\gamma\,cos\gamma-u_2\,sin^2\gamma)+\zeta_{12}(u_1-u_2)+\zeta_{23}(u_3-u_2) \quad (10)$$

$$\frac{\partial p}{\partial y}=-\frac{\mu}{K_2}v_2+\rho_0 g[\beta_T(\bar{T}-T_C)+\beta_C(\bar{C}-C_C)]+\sigma_2 B^2(u_2\,sin\lambda\,cos\lambda-v_2\,cos^2\lambda)+\zeta_{12}(v_1-v_2)+\zeta_{23}(v_3-v_2) \quad (11)$$

$$(1-\phi_1)\phi_2\rho_2 c_2\left(u_2\frac{\partial T_2}{\partial x}+v_2\frac{\partial T_2}{\partial y}\right)=(1-\phi_1)\phi_2 k_2\left(\frac{\partial^2 T_2}{\partial x^2}+\frac{\partial^2 T_2}{\partial y^2}\right)+h_{12}(T_1-T_2)+h_{23}(T_3-T_2) \quad (12)$$

$$(1-\phi_1)\phi_2\left(u_2\frac{\partial C_2}{\partial x}+v_2\frac{\partial C_2}{\partial y}\right)=(1-\phi_1)\phi_2 D_2\left(\frac{\partial^2 C_2}{\partial x^2}+\frac{\partial^2 C_2}{\partial y^2}\right)+\xi_{12}(C_1-C_2)+\xi_{23}(C_3-C_2) \quad (13)$$

Micro-pores (Size 3)

$$\frac{\partial u_3}{\partial x}+\frac{\partial v_3}{\partial y}=0 \quad (14)$$

$$\frac{\partial p}{\partial x}=-\frac{\mu}{K_3}u_3+\sigma_3 B^2(v_3\,sin\lambda\,cos\lambda-u_3\,sin^2\lambda)+\zeta_{23}(u_2-u_3) \quad (15)$$

$$\frac{\partial p}{\partial y}=-\frac{\mu}{K_3}v_3+\rho_0 g[\beta_T(\bar{T}-T_C)+\beta_C(\bar{C}-C_C)]+\sigma_3 B^2(u_3\,sin\lambda\,cos\lambda-v_3\,cos^2\lambda)+\zeta_{23}(v_2-v_3) \quad (16)$$

$$(1-\phi_1)(1-\phi_2)\rho_3 c_3\left(u_3\frac{\partial T_3}{\partial x}+v_3\frac{\partial T_3}{\partial y}\right)=(1-\phi_1)(1-\phi_2)k_3\left(\frac{\partial^2 T_3}{\partial x^2}+\frac{\partial^2 T_3}{\partial y^2}\right)+h_{23}(T_2-T_3) \quad (17)$$

$$(1-\phi_1)(1-\phi_2)\left(u_3\frac{\partial C_3}{\partial x}+v_3\frac{\partial C_3}{\partial y}\right)=(1-\phi_1)(1-\phi_2)D_3\left(\frac{\partial^2 C_3}{\partial x^2}+\frac{\partial^2 C_3}{\partial y^2}\right)+\xi_{23}(C_2-C_3) \quad (18)$$

Here, u_i and v_i are the velocity components, K_i is the permeability, ρ_i is the density, c_i is the specific heat, k_i is the thermal conductivity, and D_i is the diffusion coefficient in each scale of porosity in the TDPM. Meanwhile, ζ_{ij} is the inter-phase momentum transfer coefficient, h_{ij} is the inter-phase heat transfer coefficient, and ξ_{ij} is the inter-phase mass transfer coefficient. Notice in this formulation that the transfer terms tend to make correlation between the momentum, energy, and mass transfer of macro-pores and meso-pores as well as meso-pores and micro-pores.

After eliminating the pressure terms appearing in the momentum equations in a usual way and utilizing the following definitions for the stream function of each scale of porosity, ψ_i:

$$u_1=\frac{\partial\psi_1}{\partial y},v_1=-\frac{\partial\psi_1}{\partial x} \quad (19)$$

$$u_2=\frac{\partial\psi_2}{\partial y},v_2=-\frac{\partial\psi_2}{\partial x} \quad (20)$$

$$u_3=\frac{\partial\psi_3}{\partial y},v_3=-\frac{\partial\psi_3}{\partial x} \quad (21)$$

the following transformations are introduced to convert the equations into a dimensionless form:

$$X=\frac{x}{L},Y=\frac{y}{L},\Psi_1=\frac{\psi_1}{\phi_1\alpha_1},\Psi_2=\frac{\psi_2}{(1-\phi_1)\phi_2\alpha_2},\ \Psi_3=\frac{\psi_3}{(1-\phi_1)(1-\phi_2)\alpha_3},\Theta_1=\frac{T_1-T_C}{T_H-T_C},\Theta_2=\frac{T_2-T_C}{T_H-T_C},\ \Theta_3=\frac{T_3-T_C}{T_H-T_C},\varphi_1=\frac{C_1-C_C}{C_H-C_C},\varphi_2=\frac{C_2-C_C}{C_H-C_C},\varphi_3=\frac{C_3-C_C}{C_H-C_C} \quad (22)$$

The resulting dimensionless form of the 3V-3T-3C equations governing each scale of porosity are:

Macro-pores

$$(1+\eta_1)\left(\frac{\partial^2\Psi_1}{\partial X^2}+\frac{\partial^2\Psi_1}{\partial Y^2}\right)-\eta_1\beta_1\left(\frac{\partial^2\Psi_2}{\partial X^2}+\frac{\partial^2\Psi_2}{\partial Y^2}\right)+Ha^2\left(\frac{\partial^2\Psi_1}{\partial X^2}cos^2\lambda+2\frac{\partial^2\Psi_1}{\partial X\partial Y}sin\lambda\,cos\lambda+\frac{\partial^2\Psi_1}{\partial Y^2}sin^2\lambda\right)=-Ra\left\{\tau_1\frac{\partial\Theta_1}{\partial X}+\tau_2\frac{\partial\Theta_2}{\partial X}+(1-\tau_1-\tau_2)\frac{\partial\Theta_3}{\partial X}+Nc\left[\tau_1\frac{\partial\varphi_1}{\partial X}+\tau_2\frac{\partial\varphi_2}{\partial X}+(1-\tau_1-\tau_2)\frac{\partial\varphi_3}{\partial X}\right]\right\} \quad (23)$$

$$\phi_1\left(\frac{\partial\Psi_1}{\partial Y}\frac{\partial\Theta_1}{\partial X}-\frac{\partial\Psi_1}{\partial X}\frac{\partial\Theta_1}{\partial Y}\right)=\frac{\partial^2\Theta_1}{\partial X^2}+\frac{\partial^2\Theta_1}{\partial Y^2}+\nu_1(\Theta_2-\Theta_1) \quad (24)$$

$$\phi_1\left(\frac{\partial\Psi_1}{\partial Y}\frac{\partial\varphi_1}{\partial X}-\frac{\partial\Psi_1}{\partial X}\frac{\partial\varphi_1}{\partial Y}\right)=\frac{1}{Le_1}\left(\frac{\partial^2\varphi_1}{\partial X^2}+\frac{\partial^2\varphi_1}{\partial Y^2}\right)+\delta_1(\varphi_2-\varphi_1) \quad (25)$$

Meso-pores

$$-\eta_1\left(\frac{\partial^2\Psi_1}{\partial X^2}+\frac{\partial^2\Psi_1}{\partial Y^2}\right)+\beta_1\left(\frac{1}{K_{r1}}+\eta_1+\eta_2\right)\left(\frac{\partial^2\Psi_2}{\partial X^2}+\frac{\partial^2\Psi_2}{\partial Y^2}\right)-\beta_2\eta_2\left(\frac{\partial^2\Psi_3}{\partial X^2}+\frac{\partial^2\Psi_3}{\partial Y^2}\right)+\omega_1\beta_1 Ha^2\left(\frac{\partial^2\Psi_2}{\partial X^2}cos^2\lambda+2\frac{\partial^2\Psi_2}{\partial X\partial Y}sin\lambda\,cos\lambda+\frac{\partial^2\Psi_2}{\partial Y^2}sin^2\lambda\right)=-Ra\left\{\tau_1\frac{\partial\Theta_1}{\partial X}+\tau_2\frac{\partial\Theta_2}{\partial X}+(1-\tau_1-\tau_2)\frac{\partial\Theta_3}{\partial X}+Nc\left[\tau_1\frac{\partial\varphi_1}{\partial X}+\tau_2\frac{\partial\varphi_2}{\partial X}+(1-\tau_1-\tau_2)\frac{\partial\varphi_3}{\partial X}\right]\right\} \quad (26)$$

$$(1-\phi_1)\phi_2\left(\frac{\partial\Psi_2}{\partial Y}\frac{\partial\Theta_2}{\partial X}-\frac{\partial\Psi_2}{\partial X}\frac{\partial\Theta_2}{\partial Y}\right)=\frac{\partial^2\Theta_2}{\partial X^2}+\frac{\partial^2\Theta_2}{\partial Y^2}+\gamma_1\nu_1(\Theta_1-\Theta_2)+\gamma_2\nu_2(\Theta_3-\Theta_2) \quad (27)$$

$$(1-\phi_1)\phi_2\left(\frac{\partial\Psi_2}{\partial Y}\frac{\partial\varphi_2}{\partial X}-\frac{\partial\Psi_2}{\partial X}\frac{\partial\varphi_2}{\partial Y}\right)=\frac{1}{Le_2}\left(\frac{\partial^2\varphi_2}{\partial X^2}+\frac{\partial^2\varphi_2}{\partial Y^2}\right)+\frac{\delta_1}{\beta_1}(\varphi_1-\varphi_2)+\frac{\delta_2}{\beta_1}(\varphi_3-\varphi_2) \quad (28)$$

Micro-pores

$$\begin{aligned}&-\beta_1\eta_2\left(\frac{\partial^2\Psi_2}{\partial X^2}+\frac{\partial^2\Psi_2}{\partial Y^2}\right)+\beta_2\left(\frac{1}{K_{r2}}+\eta_2\right)\left(\frac{\partial^2\Psi_3}{\partial X^2}+\frac{\partial^2\Psi_3}{\partial Y^2}\right)\\&+\omega_2\beta_2Ha^2\left(\frac{\partial^2\Psi_3}{\partial X^2}cos^2\lambda+2\frac{\partial^2\Psi_3}{\partial X\partial Y}sin\lambda\,cos\lambda+\frac{\partial^2\Psi_3}{\partial Y^2}sin^2\lambda\right)\\&=-Ra\left\{\tau_1\frac{\partial\Theta_1}{\partial X}+\tau_2\frac{\partial\Theta_2}{\partial X}+(1-\tau_1-\tau_2)\frac{\partial\Theta_3}{\partial X}\right.\\&\left.+Nc\left[\tau_1\frac{\partial\varphi_1}{\partial X}+\tau_2\frac{\partial\varphi_2}{\partial X}+(1-\tau_1-\tau_2)\frac{\partial\varphi_3}{\partial X}\right]\right\}\end{aligned} \quad (29)$$

$$(1-\phi_1)(1-\phi_2)\left(\frac{\partial\Psi_3}{\partial Y}\frac{\partial\Theta_3}{\partial X}-\frac{\partial\Psi_3}{\partial X}\frac{\partial\Theta_3}{\partial Y}\right)=\frac{\partial^2\Theta_3}{\partial X^2}+\frac{\partial^2\Theta_3}{\partial Y^2}+\gamma_3\nu_2(\Theta_2-\Theta_3) \quad (30)$$

$$(1-\phi_1)(1-\phi_2)\left(\frac{\partial\Psi_3}{\partial Y}\frac{\partial\varphi_3}{\partial X}-\frac{\partial\Psi_3}{\partial X}\frac{\partial\varphi_3}{\partial Y}\right)=\frac{1}{Le_3}\left(\frac{\partial^2\varphi_3}{\partial X^2}+\frac{\partial^2\varphi_3}{\partial Y^2}\right)+\frac{\delta_2}{\beta_2}(\varphi_2-\varphi_3) \quad (31)$$

Here, the Rayleigh number, *Ra*, the Hartmann number, *Ha*, the double-diffusion ratio, *Nc*, and the Lewis numbers, Le_i, are defined as:

$$Ra=\frac{\rho_0 g\beta_T K_1(T_h-T_c)L}{\mu\phi_1\alpha_1},Ha=\sqrt{\frac{\sigma_1B^2K_1}{\mu}},Nc=\frac{\beta_C(C_H-C_C)}{\beta_T(T_H-T_C)},\quad Le_1=\frac{\alpha_1}{D_1},Le_2=\frac{\alpha_2}{D_2},Le_3=\frac{\alpha_3}{D_3} \quad (32)$$

Meanwhile, we arrive at the dimensionless values of the inter-phase momentum transfer coefficients, η_i, the inter-phase heat transfer coefficients, ν_i, and the inter-phase mass transfer coefficients, δ_i, as:

$$\eta_1=\frac{\zeta_{12}K_1}{\mu},\eta_2=\frac{\zeta_{23}K_1}{\mu},\nu_1=\frac{h_{12}L^2}{\phi_1k_1},\nu_2=\frac{h_{23}L^2}{(1-\phi_1)(1-\phi_2)k_1},\quad\delta_1=\frac{\xi_{12}L^2}{\phi_1\alpha_1},\delta_2=\frac{\xi_{23}L^2}{\phi_1\alpha_1} \quad (33)$$

and the shorthand volume fractions, τ_i, in the form of:

$$\tau_1=\frac{\phi_1}{\phi_1+(1-\phi_1)\phi_2+(1-\phi_1)(1-\phi_2)\phi_3} \quad (34)$$

$$\tau_2=\frac{(1-\phi_1)\phi_2}{\phi_1+(1-\phi_1)\phi_2+(1-\phi_1)(1-\phi_2)\phi_3} \quad (35)$$

The remaining dimensionless variables are:

$$\beta_1=\frac{(1-\phi_1)\phi_2\alpha_2}{\phi_1\alpha_1},\beta_2=\frac{(1-\phi_1)(1-\phi_2)\alpha_3}{\phi_1\alpha_1},\quad K_{r1}=\frac{K_2}{K_1},K_{r2}=\frac{K_3}{K_1},\quad\gamma_1=\frac{\phi_1k_1}{(1-\phi_1)\phi_2k_2},\gamma_2=\frac{(1-\phi_2)k_1}{\phi_2k_2},\gamma_3=\frac{k_1}{k_3},\quad\sigma_{r1}=\frac{\sigma_2}{\sigma_1},\sigma_{r2}=\frac{\sigma_3}{\sigma_1} \quad (36)$$

Boundary Conditions

Boundary conditions associated with Eqs. (23)-(31) are:

Left wall

$$\Psi_1=\Psi_2=\Psi_3=0\qquad\Theta_1=\Theta_2=\Theta_3=1\qquad\varphi_1=\varphi_2=\varphi_3=1 \quad (37)$$

Right wall

$$\Psi_1=\Psi_2=\Psi_3=0\qquad\Theta_1=\Theta_2=\Theta_3=0\qquad\varphi_1=\varphi_2=\varphi_3=0 \quad (38)$$

Top and bottom wall

$$\Psi_1=\Psi_2=\Psi_3=0\qquad\frac{\partial\Theta_1}{\partial y}=\frac{\partial\Theta_2}{\partial y}=\frac{\partial\Theta_3}{\partial y}=0\qquad\frac{\partial\varphi_1}{\partial y}=\frac{\partial\varphi_2}{\partial y}=\frac{\partial\varphi_3}{\partial y}=0 \quad (39)$$

Solution Methodology

The partial differential equations in the 3V-3T-3C model are highly non-linear in nature and strongly coupled through their source terms. These equations were discretized and transformed into algebraic equations utilizing the CV method. Solution of the nine algebraic equations was obtained through a line-by-line tridiagonal matrix algorithm with relaxation in an iterative procedure. The solution method was implemented in an in-house computational fluid dynamics code, which was developed in FORTRAN.

Stability and convergence of the numerical solution were assessed through monitoring changes in solution variables between successive iterations. The solution was announced converged when variations in in Ψ_1, Ψ_2, Ψ_3, Θ_1, Θ_2, Θ_3, φ_1, φ_2, and φ_3 between successive iterations dropped below the pre-defined tolerance level of 10^{-6}. Thereafter, the local values of the Nusselt and Sherwood numbers at the left wall for each scale of porosity in the TDPM were computed as:

$$Nu_1=\left|\frac{\partial\Theta_1}{\partial X}\right|_{X=0}\quad Nu_2=\left|\frac{\partial\Theta_2}{\partial X}\right|_{X=0}\quad Nu_3=\left|\frac{\partial\Theta_3}{\partial X}\right|_{X=0} \quad (40)$$

$$Sh_1 = \left|\frac{\partial \varphi_1}{\partial X}\right|_{X=0} \quad Sh_2 = \left|\frac{\partial \varphi_2}{\partial X}\right|_{X=0} \quad Sh_3 = \left|\frac{\partial \varphi_3}{\partial X}\right|_{X=0} \quad (41)$$

Then, the corresponding mean values were obtained from the following relations:

$$\overline{Nu}_1 = \int_0^1 Nu_1 dY \quad \overline{Nu}_2 = \int_0^1 Nu_2 dY \quad \overline{Nu}_3 = \int_0^1 Nu_3 dY \quad (42)$$

$$\overline{Sh}_1 = \int_0^1 Nu_1 dY \quad \overline{Sh}_2 = \int_0^1 Sh_2 dY \quad \overline{Sh}_3 = \int_0^1 Sh_3 dY \quad (43)$$

Finally, the volume-averaged mean values of the Nusselt and Sherwood numbers were found as:

$$< \overline{Nu} >= \tau_1 \overline{Nu}_1 + \tau_2 \overline{Nu}_2 + (1 - \tau_1 - \tau_2)\overline{Nu}_3 \quad (44)$$

$$< Sh >= \tau_1 Sh_1 + \tau_2 Sh_2 + (1 - \tau_1 - \tau_2)Sh_3 \quad (45)$$

Grid Independence Study

A structured rectangular grid was generated for the computational domain. The grid utilized mesh refinement near the walls, with a higher density of cells in these regions to more accurately capture boundary layer effects. A finer mesh size was used closer to the walls to resolve gradients in velocity, temperature, and concentration, tapering to a coarser mesh further away where variations are more gradual. This type of non-uniform meshing strategy with refinement at critical areas helped to improve solution accuracy while maintaining computational efficiency.

In order to conduct a grid independence study, three different grid systems having 100 × 100, 200 × 200, and 400×400 nodes were built. The outcomes in terms of the mean values of the Nusselt and Sherwood numbers for each scale of porosity are presented in Table 1. The reported results correspond to the following values of the pertinent parameters:

Ra = 1000, Ha = 10, $\gamma = \pi/4$, K_{r1} = 0.1, $K_{r2} = K_{r12}$, Nc = 1, $\phi_1 = \phi_2 = \phi_3$ = 0.4, γ_1 = 1.667, γ_2 = 1.5, γ_3 = 1, β_1 = 0.6, β_2 = 0.9, $Le_1 = Le_2 = Le_3$ = 5, $\eta_1 = \eta_2 = \nu_1 = \nu_2 = \delta_1 = \delta 2$ = 10, $\sigma_{r1} = \sigma_{-r2}$ = 1

In the light on the results presented in Table 1, the proper number of nodes to numerically solve the 3V-3T-3C model for the current flow problem was found to be 200 × 200.

Verification of the CFD Code

To justify the accuracy of the CFD code, the mean values of the Nusselt number for each scale of porosity in different situations are compared to those of Ghalambaz et al. [26] in Table 2. The comparison belongs to the cases having different values of η_1 (=η_2), β_1 (=β_2), and Kr_1 with:

Ra = 1000, Ha = 0, γ = 0, $K_{r2} = K^2_{r1}$, Nc = 0, $\phi_1 = \phi_2 = \phi_3$ = 0.4, $Le_1 = Le_2 = Le_3 = \infty$, $\nu_1 = \nu_2$ = 50, $\delta_1 = \delta_2$ = 0, $\gamma_1 = \gamma_2 = \gamma_3$ = 1, $\sigma_{r1} = \sigma_{r2}$ = 0

A high rate of consistency between the results is revealed. Meanwhile, the accuracy of this code for the solution of MHD and double-diffusive problems has been established in the previous works [29, 30, 43, 44, 48]. Hence, the CFD code is trustworthy and can be utilized to solve the 3V-3T-3C model for MHD double-diffusive free convection heat transfer in the square cavity occupied by the TDPM.

Table 1. Grid independence study[1]

Outcomes	Grid size		
	100 × 100	**200 × 200**	**400 × 400**
$\overline{Nu}_1$	1.191291	1.180093 (0.94%)	1.181393 (0.11%)
$\overline{Nu}_2$	1.124058	1.116864 (0.64%)	1.117535 (0.06%)
$\overline{Nu}_3$	1.047640	1.042088 (0.53%)	1.042609 (0.05%)
$\overline{Sh}_1$	3.017683	2.954624 (2.09%)	2.961847 (0.24%)
$\overline{Sh}_2$	2.534300	2.473477 (2.00%)	2.492597 (0.37%)
$\overline{Sh}_3$	1.915143	1.896375 (0.98%)	1.896391 (0.00%)

[1]Succesive errors (in %) are reported in the parentheses.

Table 2. Comparison of the results with the outcomes of a previous work of Ghalambaz *et al.* [26]

Case	η_1	β_1	K_{r1}	$\overline{Nu}_1$		$\overline{Nu}_1$		$\overline{Nu}_1$	
					Ghalambaz *et al.*	**Current study**	**Ghalambaz *et al.***	**Current study**	**Ghalambaz *et al.***
1	0.0001	1	0.0001	6.756120	6.777490	2.049471	2.054835	1.429088	1.435339
2	0.0001	10	0.01	6.768911	6.779051	2.051176	2.056077	1.431652	1.435755
3	0.01	1	1	7.744438	7.816390	5.603419	5.658928	7.119022	7.214223
4	0.01	10	0.0001	6.791854	6.730331	2.031839	2.049955	1.415802	1.433741
5	1	1	0.01	4.102677	4.120125	1.740419	1.749857	1.320962	1.329533
6	1	10	1	7.108932	7.127155	2.298631	2.309401	1.758999	1.771319

RESULTS AND DISCUSSION

In this section, numerical outcomes of the 3V-3T-3C model for MHD double-diffusive free convection heat transfer in the cavity depicted in Figure 1 are presented and discussed. Here, it is assumed that thermal conductivity, thermal diffusivity, and electrical conductivity of the three porosity scales of the TDPM are identical, i.e.:

$k_1 = k_2 = k_3$, $\alpha_1 = \alpha_2 = \alpha_3$, $\sigma_1 = \sigma_2 = \sigma_3$

The *base case* belongs to the following values of the pertinent parameters:

$Ra = 1000$, $Ha = 10$, $\gamma = \pi/4$, $K_{r1} = 0.1$, $K_{r2} = K^2_{r1}$, $Nc = 1$, $\phi_1 = \phi_2 = \phi_3 = 0.4$, $Le_1 = Le_2 = Le_3 = Le = 5$, $\eta_1 = \eta_2 = \nu_1 = \nu_2 = \delta_1 = \delta_2 = 10$, $\sigma_{r1} = \sigma_{r2} = 1$

It is noteworthy that according to Eq. (36), the values of γ_1, γ_2, β_1, and β_2 are dependent to the macro-porosity, meso-porosity, and micro-porosity of the TDPM. Hence, for the base case having $\phi_1 = \phi_2 = \phi_3 = 0.4$, one has:

$\gamma_1 = 1.667$, $\gamma_2 = 1.5$, $\gamma_3 = 1$, $\beta_1 = 0.6$, $\beta_2 = 0.9$

Simulation results of the base case in terms of the distributions of streamlines, isothermal lines, and iso-concentration lines in the macro-pores, meso-pores, and micro-pores of the TDPM are provided in Figure 2. Here and henceforth, the contour plots are streamlines, the solid lines are isothermal lines, and the dot-dash lines are iso-concentration lines. Meanwhile, the provided legends belong to the values of the stream function. Inspection of the figure elaborates that in all scales of porosity, the elevated temperature and concentration move up the fluid near the left wall. The fluid changes its direction when reaching the top wall. Finally, deterioration in the temperature and concentration at the right wall moves the fluid downward. Hence, in each scale of porosity of the TDPM, a large clockwise rotating cell is formed in the cavity. It is perceived that as one proceeds from the macro-pores to the micro-pores, the isothermal lines and iso-concentration lines become more vertical in the cavity and the level of stream function diminishes.

In what concerns the numerical values of $|\Psi_{max}|$ as well as the mean values of the Nusselt and Sherwood numbers, simulation results of the base case are reported in Table 3. Here, $|\Psi_{max}|$ stands for the flow strength. It is evident that the flow strength as well as the heat and mass transfer in the micro-pores are not as intense as what occurring in the macro-pores and meso-pores of the TDPM, which is expected.

In the following section, we deal with the features of the externally applied magnetic field as well as the effects of the numerical values of the double-diffusion ratio, the Lewis number, the macro-porosity, the meso-porosity, and the micro-porosity on the simulation results.

Effect of Magnetic Field

To scrutinize the consequence of the externally applied magnetic field on the simulation results, computations are undertaken for a case having no magnetic field (i.e., $Ha = 10$), maintaining other pertinent parameters similar to the base case. The corresponding outcomes are portrayed in Figure 3. The main contribution of the elimination of the magnetic field is seen to distort the streamlines, isothermal lines, and iso-concentration lines.

Representative outcomes illustrating the numerical values of $|\Psi_{i,max}|$, $\overline{Nu}_i$, $\overline{Sh}_i$, $<\overline{Nu}>$, and $<\overline{Sh}>$ in Table 3 for the case having $Ha = 10$ (Case 2) demonstrate that the elimination of the magnetic field intensifies the flow strength and improves the heat and mass transfer, in all scales of porosity of the TDPM. Specifically, with this alternation, the flow strength promotes 286%, 181%, and 32% in the macro-pores, meso-pores, and micro-pores, respectively. Meanwhile, the resulting Nusselt numbers boost up 186%, 86%, and 16%, respectively. Additionally, the rates of elevation in the Sherwood numbers are 276%, 182%, and 60%, respectively. This behavior is not surprising since when a magnetic field is applied, the Lorentz force tends to decline the fluid motion, which is accompanied by deterioration in the heat and mass transfer in this free

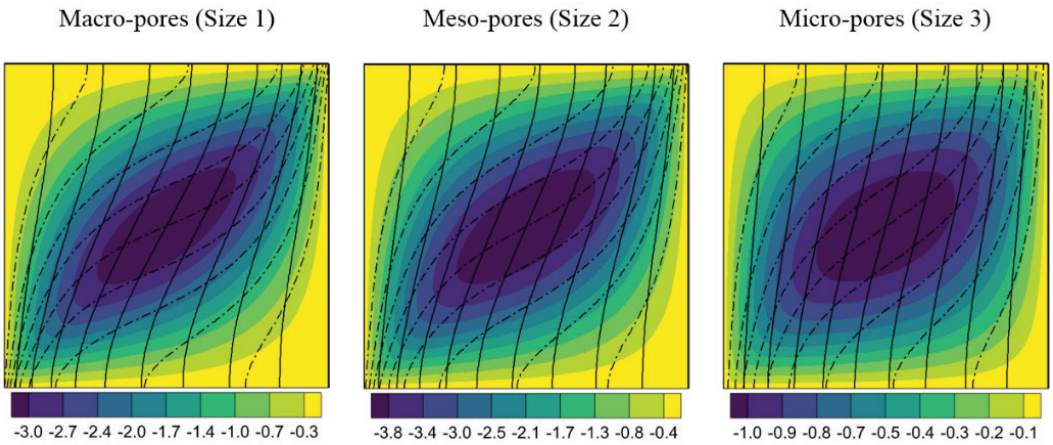

Figure 2. Simulation results for the base case (Case 1).

Table 3. The flow strength as well as the mean values of the Nusselt and Sherwood numbers in the macro-pores, meso-pores, and micro-pores for several cases.

Parameter	Case number						
	1 (Base case)	2	3	4	5	6	7
Ha	10	0	10	10	10	10	10
NC	1	1	10	1	1	1	1
Le	5	5	5	10	5	5	5
ϕ_1	0.4	0.4	0.4	0.4	0.6	0.4	0.4
ϕ_2	0.4	0.4	0.4	0.4	0.4	0.6	0.4
ϕ_3	0.4	0.4	0.4	0.4	0.4	0.4	0.6
$\lvert\Psi_{1,max}\rvert$	3.378	13.039	9.526	2.811	3.009	3.351	3.387
$\lvert\Psi_{2,max}\rvert$	4.247	11.953	11.377	3.588	8.557	2.808	4.259
$\lvert\Psi_{3,max}\rvert$	1.093	1.449	2.831	0.949	2.220	1.626	1.097
$\overline{Nu}_1$	1.180	3.371	2.353	1.141	1.342	1.181	1.180
$\overline{Nu}_2$	1.117	2.079	1.925	1.092	1.250	1.124	1.117
$\overline{Nu}_3$	1.042	1.208	1.335	1.032	1.087	1.043	1.042
$<\overline{Nu}>$	1.135	2.578	2.035	1.106	1.297	1.142	1.128
$\overline{Sh}_1$	2.954	11.110	8.697	4.565	3.900	2.985	2.956
$\overline{Sh}_2$	2.473	6.973	7.228	3.816	3.236	2.544	2.475
$\overline{Sh}_3$	1.896	3.039	4.233	2.844	2.507	2.009	1.899
$<\overline{Sh}>$	2.613	8.361	7.427	4.019	3.620	2.690	2.554

convection environment. Inspection of the alternations of the discussed parameters in the current scales of porosity elaborates that the effect of the magnetic field imposition is more intense in the macro-pores and less intense in the micro-pores. Physical reasoning for this behavior is the fact that the velocity magnitudes are much higher in the macro-pores, elevating the Lorenz force there.

Effect of the Double-diffusion Ratio

To clarify the effect of the double-diffusion ratio on the outcomes, simulation results corresponding to a case having $NC = 10$ are plotted in Figure 4. Other pertinent parameters are similar to the base case. Comparison of the outcomes with those in Figure 2 demonstrates the prominent consequence of the double-diffusion ratio on the streamlines, isothermal lines, and iso-concentration lines.

Scrutiny of the numerical results illustrated in Table 3 for the case having $NC = 10$ (Case 3) suggests that the rise in the double-diffusion ratio is accompanied by intensification in the flow strength and improvement in the heat and mass transfer, in all scales of porosity of the TDPM. Notice that owing to the tenfold increase in NC, the flow strength

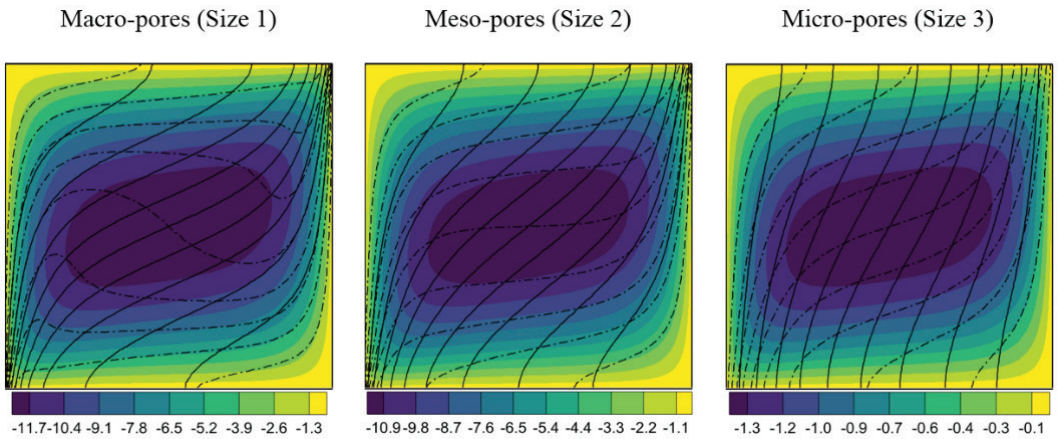

Figure 3. Simulation results for the case having $Ha = 10$ (Case 2).

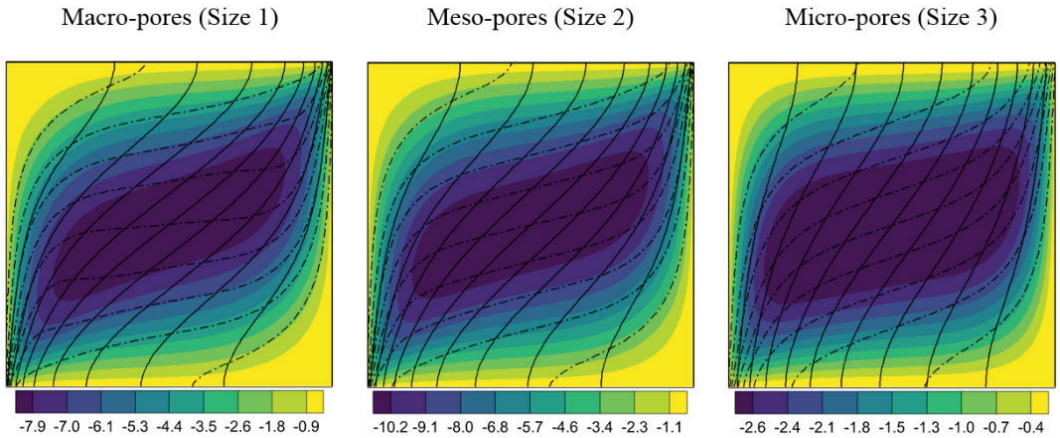

Figure 4. Simulation results for the case having *NC* = 10 (Case 3).

elevates 182%, 168%, and 159% in the macro-pores, meso-pores, and micro-pores, respectively. Meanwhile, the resulting Nusselt number has a tendency to improve 99%, 72%, and 28%, respectively. Additionally, the rates of elevation in the Sherwood number are 194%, 192%, and 123%, respectively. Similar to the magnetic field, notice that the effect of the double-diffusion ratio is more intense in the macro-pores and less intense in the micro-pores.

Effect of the Lewis Number

Figure 5 is constructed to enlighten the effect of the Lewis number on the streamlines, isothermal lines, and iso-concentration lines. Here, simulation results for a case having *Le* = 10 are plotted, maintaining other pertinent parameters similar to the base case. Comparison of the outcomes with those in Figure 2 implies that the highest impact of the Lewis number belongs to the iso-concentration lines. This is expected since this parameter appears in the solute concentration equations.

The numerical outcomes reported in Table 3 for the case having *Le* = 10 (Case 4) elaborate that the twofold rise in the Lewis number causes small retardations in the flow strength and heat transfer and substantial elevation in the mass transfer, in all scales of porosity of the TDPM. Specifically, the twofold increase in *Le* participates in 17%, 16%, and 13% deteriorations in the flow strength in the macro-pores, meso-pores, and micro-pores, respectively. Meanwhile, the resulting Nusselt number diminishes 3%, 2%, and 0.9%, respectively. However, the rates of promotion in the Sherwood number are 55%, 54%, and 50%, respectively. Again, notice that the effect of the analyzed parameter is more intense in the macro-pores and less intense in the micro-pores.

Effect of the Porosities

It is interesting to disclose the features of the macro-porosity, meso-porosity, and micro-porosity of the TDPM on the simulation results. Accordingly, the streamlines, isothermal lines, and iso-concentration lines for the cases

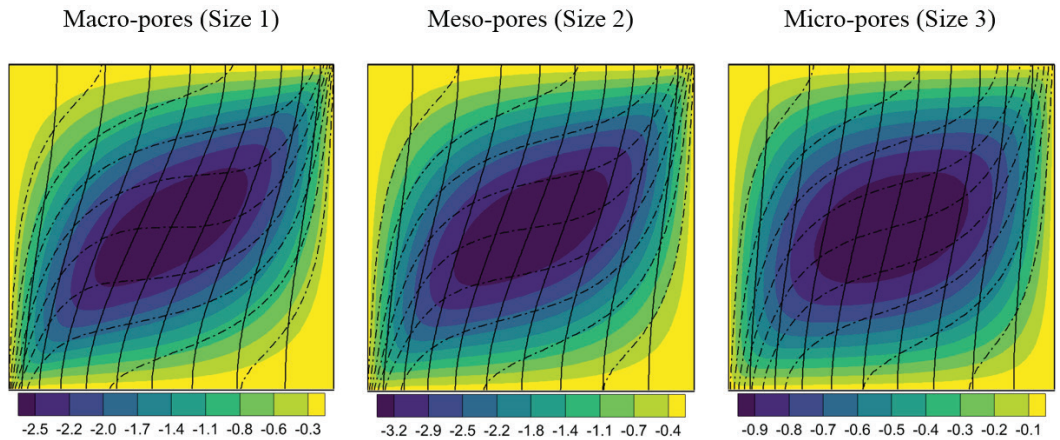

Figure 5. Simulation results for the case having *Le* = 10 (Case 4).

having $\phi_1 = 0.6$, $\phi_2 = 0.6$, or $\phi_3 = 0.6$ are plotted in Figure 6. To arrive at these results, other pertinent parameters are taken similar to the base case. It should be mentioned that, according to Eq. (36), any alternation in the porosities of the TDPM is accompanied by change in the values of γ_1, γ_2, β_1, and β_2. It is evident from Figure 6 that the assisted porosities have no tangible effect on the distribution of streamlines, isothermal lines, and iso-concentration lines.

The numerical results illustrated in Table 3 for the case having $\phi_1 = 0.6$ (Case 5) evidently point out that the rise in the macro-porosity leads to small reduction in $|\Psi_{max}|$ in the macro-pores and substantial elevation in the flow strength in the meso-pores and micro-pores. This also improves the heat and mass transfer in all scales of porosity of the TDPM. Specifically, as a result of passing from $\phi_1 = 0.4$ to $\phi_1 = 0.6$, the flow strength deteriorates 11% in the macro-pores and elevates 101%, and 103% in meso-pores and micro-pores,

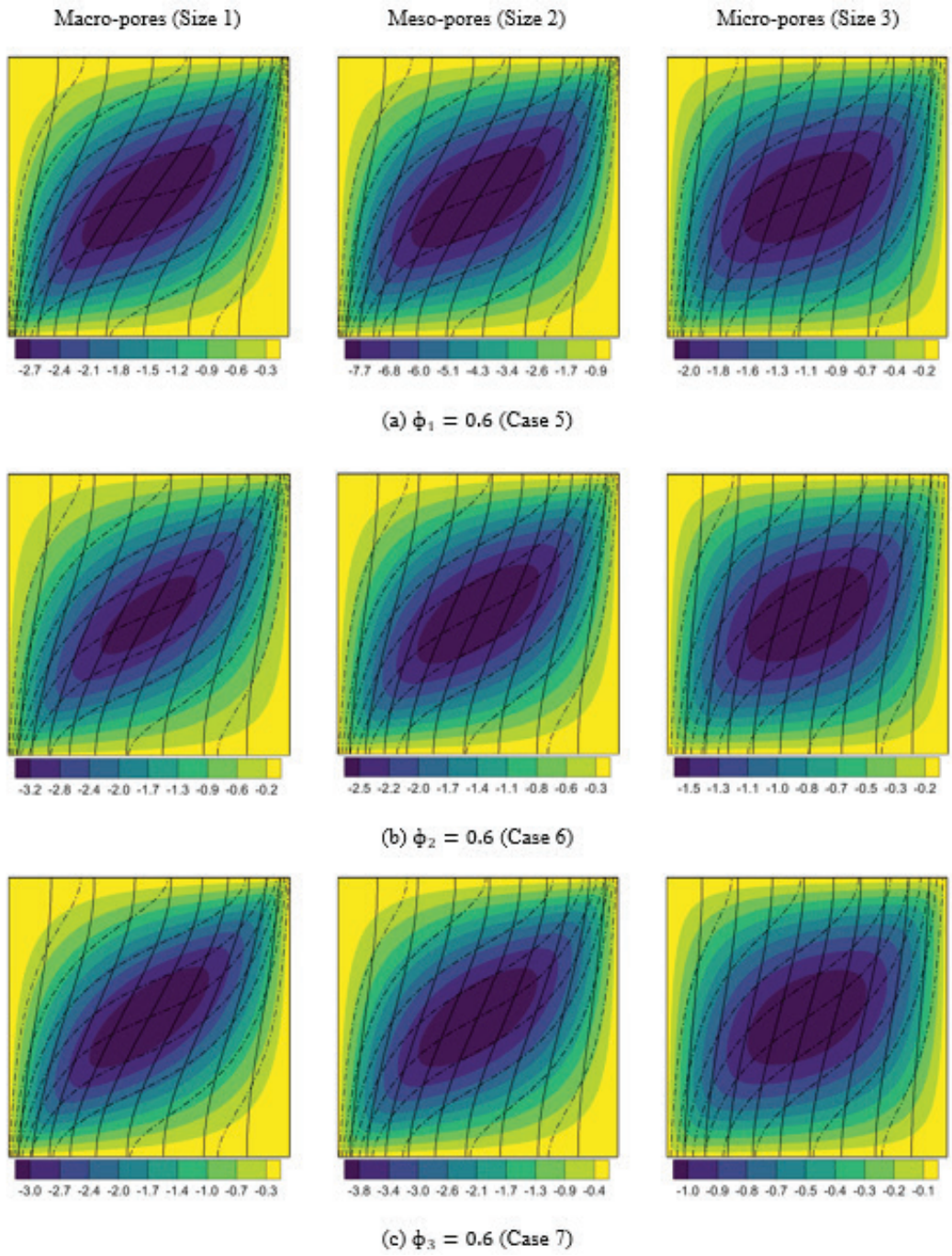

Figure 6. Effect of the macro-porosity, meso-porosity, and micro-porosity on the simulation results.

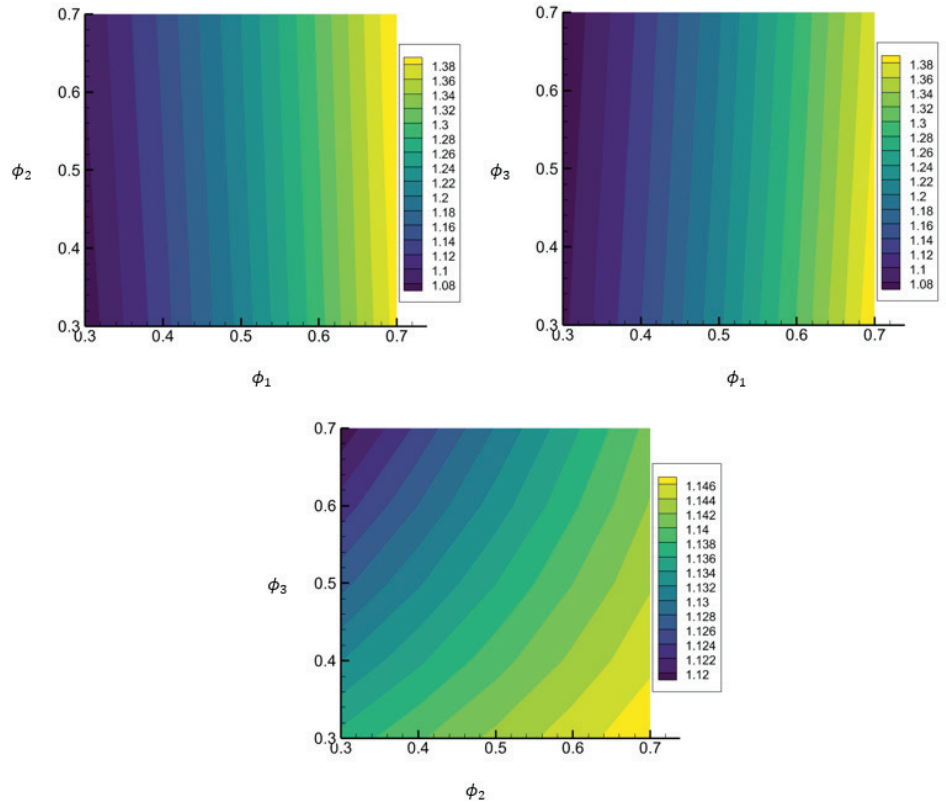

Figure 7. Dependence of the volume-averaged mean value of the Nusselt number to the macro-porosity, meso-porosity, and micro-porosity.

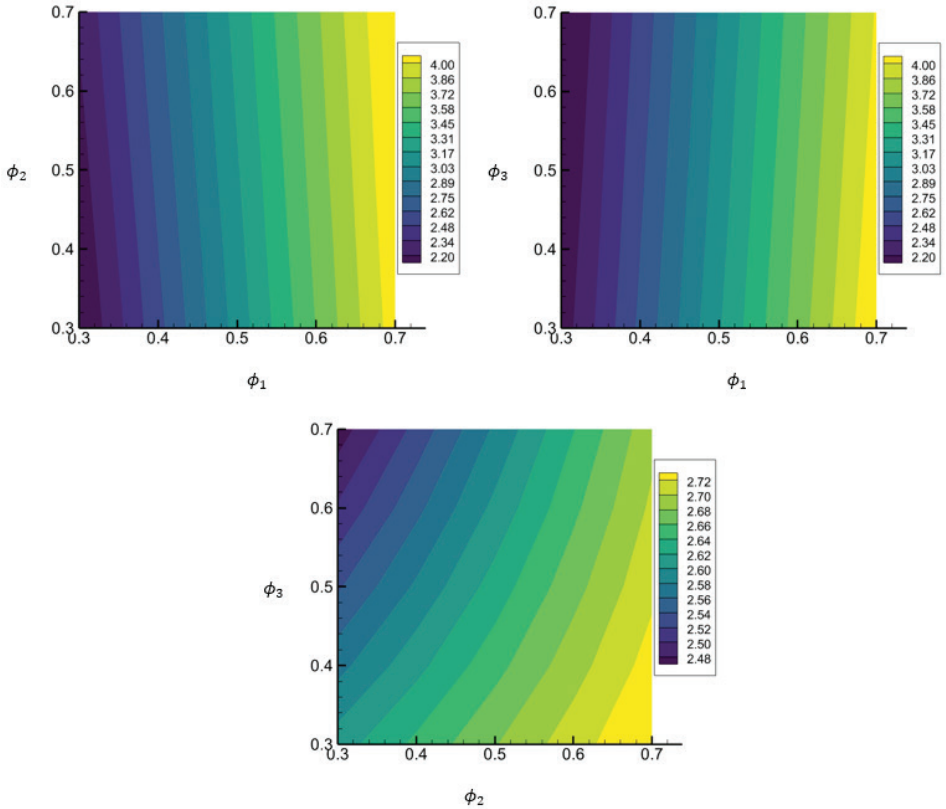

Figure 8. Dependence of the volume-averaged mean value of the Sherwood number to the macro-porosity, meso-porosity, and micro-porosity.

respectively. Meanwhile, the resulting Nusselt number has a tendency to improve 14%, 12%, and 4%, respectively. However, the rates of elevation in the Sherwood number are 32%, 31%, and 32%, respectively. It is also obvious that rising ϕ_2 from 0.4 to 0.6 (Case 6) results in 34% deterioration in $|\Psi_{max}|$ in the meso-pores and 49% elevation in the flow strength in the micro-pores. However, this effect has not changed the other parameters more than 6%. It is also evident that the alternation of the results owing to the increment in ϕ_3 (Case 7) may not exceed 2%. Notice that, in contrast to the previous effects, no general conclusion can be drawn about the consequences of the porosities of the TDPM on the outcomes of different porosity scales.

To provide a better picture about the effect of the macro-porosity, meso-porosity, and micro-porosity of the TDPM on the heat and mass transfer performances, the dependence of the volume-averaged mean values of the Nusselt and Sherwood numbers to the macro-porosity, meso-porosity, and micro-porosity are portrayed in Figures 7 and 8, respectively. It is clear that change in the macro-porosity is more likely to alter the heat and mass transfer performances, as compared with the meso-porosity and micro-porosity. The results also show that growth of the macro-porosity and meso-porosity or deterioration in the micro-porosity leads to improvement in the heat and mass transfer characteristics.

CONCLUSION

The present study was pursued to scrutinize MHD double-diffusive free convection heat transfer in a square cavity occupied by a TDPM. To this aim, a three-velocity three-temperature three-concentration (3V-3T-3C) model was developed to describe the momentum, energy, and mass transfer in the macro-pores, meso-pores, and micro-pores of the TDPM. The model also incorporated the contribution of magnetic field imposition with an arbitrary angle of the magnetic field. The main results may be stated as:

(1) The elimination of the magnetic field tends to improve the Nusselt and Sherwood numbers, in all scales of porosity of the TDPM. Specifically, with this alternation, the Nusselt numbers boost up 186%, 86%, and 16% in the macro-pores, meso-pores, and micro-pores, respectively. Meanwhile, the rates of elevation in the Sherwood numbers are 276%, 182%, and 60%, respectively.
(2) In all scales of porosity of the TDPM, an increment in the double-diffusion ratio has a tendency to boost up the Nusselt and Sherwood numbers. Specifically, with a tenfold increase in the double-diffusion ratio, the Nusselt number improves 99%, 72%, and 28%, in the macro-pores, meso-pores, and micro-pores, respectively. Meanwhile, the rates of elevation in the Sherwood number are 194%, 192%, and 123%, respectively.
(3) Rise in the Lewis number is accompanied by small reduction in the Nusselt number and substantial elevation in the Sherwood number, in all scales of porosity of the TDPM. Specifically, the twofold increase in the Lewis number participates in 3%, 2%, and 0.9%, deteriorations in the Nusselt number in the macro-pores, meso-pores, and micro-pores, respectively. Meanwhile, the rates of promotion in the Sherwood number are 55%, 54%, and 50%, respectively.
(4) The effects of the magnetic field imposition, the double-diffusion ratio, and the Lewis number are more intense in the macro-pores and less intense in the micro-pores.
(5) The contribution of the macro-porosity of the TDPM on the Nusselt and Sherwood numbers is more significant than the meso-porosity and micro-porosity.
(6) Growth of the macro-porosity and meso-porosity of the TDPM leads to improvement in the Nusselt and Sherwood numbers.
(7) With deterioration in the micro-porosity of the TDPM, higher values of the Nusselt and Sherwood numbers can be achieved.

In this work, the performed grid independence quantified the numerical uncertainty due to spatial discretization. While this removed one source of uncertainty, the study did not characterize other sources such as those from modeling assumptions, empirical relationships, and approximates made in developing the 3V-3T-3C model. A more rigorous uncertainty quantification approach is needed to propagate the effects of input parameter and modeling uncertainties through the simulations. This would further strengthen confidence in the results. While the current study provided a useful first assessment of the new model, fully characterizing prediction uncertainties remains an important goal for future work. More rigorous uncertainty analysis could help establish the reliability of using this 3V-3T-3C model for future applications.

NOMENCLATURE

B	magnetic field strength (T)
c_1, c_2, c_3	Specific heat in each scale of porosity ($Jkg^{-1}K^{-1}$)
C_1, C_2, C_3	Solute concentration in each scale of porosity
$\bar{C}$	Volume-averaged concentration
D_1, D_2, D_3	Diffusion coefficient in each scale of porosity ($m^2\ s^{-1}$)
$\hat{e}_x, \hat{e}_y$	Unit vectors in the Cartesian coordinate system
g	Gravitational acceleration (ms^{-2})
Ha	Hartmann number
h_{12}, h_{23}	Inter-phase heat transfer coefficient ($Wm^{-3}\ K^{-1}$)
k_1, k_2, k_3	Thermal conductivity in each scale of porosity ($Wm^{-1}\ K^{-1}$)
K_1, K_2, K_3	Permeability in each scale of porosity (m^2)
K_{r1}, K_{r2}	Defined in Eq. (36)
L	Size of the cavity (m)
Le_1, Le_2, Le_3	Lewis number in each scale of porosity

Nc	Double-diffusion ratio
Nu_1, Nu_2, Nu_3	Local Nusselt number in each scale of porosity
$\overline{Nu}_1$, $\overline{Nu}_2$, $\overline{Nu}_3$	Mean Nusselt number in each scale of porosity
$< \overline{Nu} >$	Volume-averaged mean value of the Nusselt number
P	Pressure (Pa)
Ra	Rayleigh number based on properties of the macro-pores
Sh_1, Sh_2, Sh_3	Local Sherwood number in each scale of porosity
$\overline{Sh}_1$, $\overline{Sh}_2$, $\overline{Sh}_3$	Mean Sherwood number in each scale of porosity
$< \overline{Sh} >$	Volume-averaged mean value of the Sherwood number
T_1, T_2, T_3	Temperature in each scale of porosity (K)
$\overline{T}$	Volume-averaged temperature (K)
u_1, u_2, u_3	Horizontal velocity component in each scale of porosity (ms^{-1})
v_1, v_2, v_3	Vertical velocity component in each scale of porosity (ms^{-1})
V_1, V_2, V_3	Velocity vector in each scale of porosity
x,y	Cartesian coordinates (m)
X, Y	Dimensionless Cartesian coordinates

Greek symbols

α_1, α_2, α_3	Thermal diffusivity in each scale of porosity ($m^2\ s^{-1}$)
β_1, β_2	Defined in Eq. (36)
β_C	Solute concentration expansion coefficient
β_T	Thermal expansion coefficient (K^{-1})
γ_1, γ_2, γ_3	Defined in Eq. (36)
δ_1, δ_2	Dimensionless inter-phase mass transfer coefficient
ζ_{12}, ζ_{23}	Inter-phase momentum transfer coefficient (Nsm^{-4})
η_1, η_2	Dimensionless inter-phase momentum transfer coefficient
Θ_1, Θ_2, Θ_3	Dimensionless temperature
λ	Magnetic field inclination angle
μ	Dynamic viscosity (Nsm^{-2})
ν_1, ν_2	Dimensionless inter-phase heat transfer coefficient
ξ_{12}, ξ_{23}	Inter-phase mass transfer coefficient (s^{-1})
ρ_1, ρ_2, ρ_3	Density in each scale of porosity (kgm^{-3})
ρ_0	Reference fluid density (kgm^{-3})
σ_1, σ_2	Electrical conductivity ($\Omega^{-1}\ m^{-1}$)
σ_{r1}, σ_{r2}	Defined in Eq. (36)
τ_1, τ_2	Shorthand volume fraction
ϕ_1	Macro-porosity
ϕ_2	Meso-porosity
ϕ_3	Micro-porosity
φ_1, φ_2, φ_3	Dimensionless solute concentration in each scale of porosity
ψ_1, ψ_2, ψ_3	Stream function in each scale of porosity ($m^2\ s^{-1}$)
Ψ_1, Ψ_2, Ψ_3	Dimensionless stream function in each scale of porosity

Subscripts

C	Cold
H	Hot

DATA AVAILABILITY STATEMENT

The authors confirm that the data that supports the findings of this study are available within the article. Raw data that support the finding of this study are available from the corresponding author, upon reasonable request.

CONFLICT OF INTEREST

The author declared no potential conflicts of interest with respect to the research, authorship, and/or publication of this article.

ETHICS

There are no ethical issues with the publication of this manuscript.

REFERENCES

[1] Narasimhan A, Reddy BVK, Dutta P. Thermal management using the bi-disperse porous medium approach. Int J Heat Mass Transf 2012;55:538−546. [CrossRef]

[2] Chen ZQ, Cheng P, Zhao TS. An experimental study of two phase flow and boiling heat transfer in bi-dispersed porous channels. Int Comm Heat Mass Transf 2000;27:293−302. [CrossRef]

[3] Nield DA, Kuznetsov AV. Forced convection in a bi-disperse porous medium channel: A conjugate problem. Int J Heat Mass Transf 2004;47:5375−5380. [CrossRef]

[4] Nield D, Kuznetsov AV. A two-velocity two-temperature model for a bi-dispersed porous medium: Forced convection in a channel. Transp Porous Med 2005;59:325−339. [CrossRef]

[5] Nield DA, Kuznetsov AV. Thermally developing forced convection in a bidisperse porous medium. J Porous Med 2006;9:393−402. [CrossRef]

[6] Nield DA, Kuznetsov AV. The onset of convection in a bidisperse porous medium. Int J Heat Mass Transf 2006;49:3068−3074. [CrossRef]

[7] Nield DA, Kuznetsov AV. The effect of combined vertical and horizontal heterogeneity on the onset of convection in a bidisperse porous medium. Int J Heat Mass Transf 2007;50:3329−3339. [CrossRef]

[8] Nield DA, Kuznetsov AV. Natural convection about a vertical plate embedded in a bidisperse porous medium. Int J Heat Mass Transf 2008;51:1658−1664. [CrossRef]

[9] Kuznetsov A, Nield D. Forced convection in a channel partly occupied by a bidisperse porous medium: Symmetric case. Int J Heat Mass Transf 2010;53:5167−5175. [CrossRef]
[10] Rees DAS, Nield D, Kuznetsov AV. Vertical free convective boundary-layer flow in a bidisperse porous medium. J Heat Transf 2008;130:092601. [CrossRef]
[11] Cheng CY. Natural convection heat transfer from an inclined wavy plate in a bidisperse porous medium. Int Comm Heat Mass Transf 2013;43:69−74. [CrossRef]
[12] Revnic C, Grosan T, Pop I, Ingham DB. Free convection in a square cavity filled with a bidisperse porous medium. Int J Therm Sci 2009;48:1876−1883. [CrossRef]
[13] Narasimhan A, Reddy BVK. Natural convection inside a bidisperse porous medium enclosure. J Heat Transf 2010;132:012502. [CrossRef]
[14] Wang K, Vafai K, Cen H. Forced convection in a bidisperse porous medium embedded in a circular pipe. J Heat Transf 2017;139:102601. [CrossRef]
[15] Straughan B. Anisotropic bidispersive convection. Proc R Soc A 2019;475:20190206. [CrossRef]
[16] Capone F, De Luca R. The effect of the Vadasz number on the onset of thermal convection in rotating bidispersive porous media. Fluids 2020;5:173. [CrossRef]
[17] Capone F, De Luca R. Instability of vertical throughflows in bidisperse porous media. Phys 2021;3:821−828. [CrossRef]
[18] Wang K, Wang Q, Li P. Forced convection in a fully-filled bidisperse porous annular duct subject to asymmetric heat fluxes. Therm Sci Engineer Prog 2022;32:101328. [CrossRef]
[19] Siddabasappa C, Siddheshwar PG, Mallikarjunaiah SM. Analytical study of Brinkman-Bénard convection in a bidisperse porous medium: Linear and weakly nonlinear study. Therm Sci Engineer Prog 2023;39:101696. [CrossRef]
[20] Meza LR, Das S, Greer JR. Strong, lightweight, and recoverable three-dimensional ceramic nanolattices. Sci 2014;345:1322−1326. [CrossRef]
[21] Rys J, Valdevit L, Schaedler TA, Jacobsen AJ, Carter WB, Greer JR. Fabrication and deformation of metallic glass micro-lattices. Adv Engineer Math 2014;16:889−896. [CrossRef]
[22] Nield DA, Kuznetsov AV. A three-velocity three-temperature model for a tridisperse porous medium: Forced convection in a channel. Int J Heat Mass Transf 2011;54:2490−2498. [CrossRef]
[23] Kuznetsov A, Nield D. The onset of convection in a tridisperse porous medium. Int J Heat Mass Transf 2011;54:3120−3127. [CrossRef]
[24] Nield DA, Kuznetsov AV. The Cheng-Minkowycz problem for natural convection about a vertical plate embedded in a tridisperse porous medium. Int J Heat Mass Transf 2011;54:3485−3493. [CrossRef]
[25] Cheng CY. Natural convection heat transfer about a vertical cone embedded in a tridisperse porous medium. Transp Porous Med 2015;107:765−779. [CrossRef]
[26] Ghalambaz M, Hendizadeh H, Zargartalebi H, Pop I. Free convection in a square cavity filled with a tridisperse porous medium. Transp Porous Med 2017;116:379−392. [CrossRef]
[27] Umavathi J, Sheremet M. Onset of double-diffusive convection of a sparsely packed micropolar fluid in a porous medium layer saturated with a nanofluid. Microfluid Nanofluid 2017;21:128. [CrossRef]
[28] Aly AM, Mohamed E, El-Amin M, Alsedais N. Double-diffusive convection between two different phases in a porous infinite-shaped enclosure suspended by nano encapsulated phase change materials. Case Stud Therm Engineer 2021;26:101016. [CrossRef]
[29] Habibi MR, Zahmatkesh I. Double-diffusive natural and mixed convection of binary nanofluids in porous cavities. J Porous Med 2020;23:955−967. [CrossRef]
[30] Zahmatkesh I, Shandiz MRH. MHD double-diffusive mixed convection of binary nanofluids through a vertical porous annulus considering Buongiorno's two-phase model. J Therm Anal Calorim 2022;147:1793−1807. [CrossRef]
[31] Ghalambaz M, Moattar F, Sheremet M, Pop I. Triple-diffusive natural convection in a square porous cavity. Transp Porous Med 2016;111:59−79. [CrossRef]
[32] Ghalambaz M, Moattar F, Karbassi AR, Sheremet M, Pop I. Triple-diffusive mixed convection in a porous open cavity. Transp Porous Med 2017;116:473−491. [CrossRef]
[33] Khan Z, Khan W, Sheremet M. Enhancement of heat and mass transfer rates through various porous cavities for triple convective-diffusive free convection. Energy 2020;201:117702. [CrossRef]
[34] Straughan B. Effect of inertia on double diffusive bidispersive convection. Int J Heat Mass Transf 2019;129:389−396. [CrossRef]
[35] Wang Q, Wang K. Forced convective heat and mass transfer in a bidisperse porous parallel-plate channel with a first order reaction on the wall. Therm Sci Engineer Prog 2019;13:100369. [CrossRef]
[36] Badday AJ, Harfash AJ. Double-diffusive convection in bidispersive porous medium with chemical reaction and magnetic field effects. Transp Porous Med 2021;139:45−66. [CrossRef]
[37] Badday AJ, Harfash AJ. Thermosolutal convection in a bidisperse porous medium with chemical reaction effect and relatively large macropores. J Porous Med 2023;26:31−49. [CrossRef]
[38] Ramchandraiah C, Kishan N, Reddy GSK, Paidipati KK, Chesneau C. Double-diffusive convection in bidispersive porous medium with coriolis effect. Math Comp Appl 2022;27:56. [CrossRef]

[39] Wakif A, Boulahia Z, Sehaqui R. Numerical analysis of the onset of longitudinal convective rolls in a porous medium saturated by an electrically conducting nanofluid in the presence of an external magnetic field. Results Phys 2017;7:2134−2152. [CrossRef]

[40] Sheremet MA, Astanina MS, Pop I. MHD natural convection in a square porous cavity filled with a water-based magnetic fluid in the presence of geothermal viscosity. Int J Numeri Meth Heat Fluid Flow 2018;28:2111−2131. [CrossRef]

[41] Krishna MV, Chamkha AJ. Hall and ion slip effects on MHD rotating boundary layer flow of nanofluid past an infinite vertical plate embedded in a porous medium. Results Phys 2019;15:102652. [CrossRef]

[42] Ghalambaz M, Sabour M, Pop I, Wen D. Free convection heat transfer of MgO-MWCNTs/EG hybrid nanofluid in a porous complex shaped cavity with MHD and thermal radiation effects. Int J Numeri Meth Heat Fluid Flow 2019;29:4349−4376. [CrossRef]

[43] Zahmatkesh I, Shandiz MRH. Optimum constituents for MHD heat transfer of nanofluids within porous cavities. J Therm Anal Calorim 2019;138:1669−1681. [CrossRef]

[44] Zahmatkesh I, Ardekani RA. Effect of magnetic field orientation on nanofluid free convection in a porous cavity: a heat visualization study. J Therm Engineer 2020;6:170−186. [CrossRef]

[45] Ragupathi P, Muhammad T, Islam S, Wakif. Application of Arrhenius kinetics on MHD radiative Von Kármán Casson nanofluid flow occurring in a Darcy-Forchheimer porous medium in the presence of an adjustable heat source. Phys Script 2021:96:125228. [CrossRef]

[46] Ouni M, Selimefendigil F, Hatem B, Kolsi L, Omri M. Utilization of wavy porous layer, magnetic field and hybrid nanofluid with slot jet impingement on the cooling performance of conductive panel. Int J Numeri Meth Heat Fluid Flow 2023;33:360−384. [CrossRef]

[47] Paul A, Nath JM, Das TK. An investigation of the MHD Cu-Al2O3/H2O hybrid-nanofluid in a porous medium across a vertically stretching cylinder incorporating thermal stratification impact. J Therm Engineer 2023;9:799−810. [CrossRef]

[48] Zahmatkesh I. On the importance of thermal boundary conditions in heat transfer and entropy generation for natural convection inside a porous enclosure. Int J Therm Sci 2008;47:339−346. [CrossRef]